ADVANCED SUSTAINABLE SYSTEMS
www.advsustainsys.com

Nanosizing Ammonia Borane with Nickel: A Path toward the Direct Hydrogen Release and Uptake of B—N—H Systems

*Qiwen Lai, Aditya Rawal, Md Zakaria Quadir, Claudio Cazorla, Umit B. Demirci, and Kondo-Francois Aguey-Zinsou**

Ammonia borane (AB), with one of the highest hydrogen content (19.6 mass%), has attracted much attention as a potential hydrogen storage material. However, its complex and multistep thermal decomposition process has left the idea that AB can only be an irreversible hydrogen storage material. Herein, we demonstrate the potential of a novel nanosizing strategy in overcoming current drawbacks. By (a) successfully restricting the particle size of AB to the nanoscale (≈50 nm), and (b) discreetly encapsulating the synthesised nanosized AB particles within a nickel (Ni) matrix, AB showed unforeseen hydrogen reversibility along its decomposition path. Owing to the catalytic effect of Ni and the embedment of AB with the Ni matrix, this nanosizing approach reduced the hydrogen release temperature, suppressed the melting of AB and the production of volatiles by-products including diborane and borazine. But more remarkably, this approach enabled the reversible release and uptake of pure hydrogen at 200 °C and 6 MPa H_2 pressure, only. Reversibility is thought to occur through an iminoborane oligomer resulting from the initial decomposition of the nanosized AB/Ni matrix. This result demonstrates for the first time the possibility of tailoring.

1. Introduction

Ammonia borane (NH_3BH_3, AB) is believed to be a promising hydrogen storage material with one of the highest hydrogen content (19.6 mass%). AB has a large polarity due to the electronegativity differences between B (2.04) and N (3.04).[1] BH_3 acts as a Lewis acid, NH_3 as a Lewis base, and both moieties form a dative covalent bond. The existence of dihydrogen bonding between protic (N—H) and hydridic (B—H) hydrogens leads not only to enormously high volumetric (145 kg L^{-1}) and gravimetric density but also favors hydrogen release at low temperatures.

AB can release hydrogen through hydrolysis and thermolysis; and various attempts have been made to effectively extract hydrogen from both routes.[2–6] The activation energy for AB hydrolysis was measured to be between 21 and 87 kJ mol^{-1},[7] compared to values ranging from 69.6 to 184 kJ mol^{-1} for thermolysis.[1,8–11] Hence, the hydrolysis route following (1a) and/or (1b) is easier to activate with the assistance of a metal-based catalyst[12–20]

$$NH_3BH_3 + 3H_2O \rightarrow NH_3 + B(OH)_3 + 3H_2 \quad (1a)$$

$$NH_3BH_3 + 4H_2O \rightarrow NH_4^+ + B(OH)_4^- + 3H_2 \quad (1b)$$

However, following (1a) and (1b) the maximum amount of hydrogen released is limited to 7.1 and 5.8 mass%, respectively owing to the remaining hydrogen in the NH_3/NH_4^+ products,[21] and this capacity is even lower in practical systems when considering any excess of H_2O. The hydrolysis route also suffers from two major issues. In addition to the concomitant release of ammonia (NH_3) with hydrogen, the hydrolysis of AB is highly exothermic (≈−227 kJ mol^{-1}) owing to the bond strength difference between B—O and B—N.[5] It is thus very difficult to regenerate NH_3BH_3 from its hydrolyzed borate products, i.e., $B(OH)_3/B(OH)_4^-$.

On the other hand the thermolysis of AB is a solid–gas reaction with potential of releasing a larger amount of hydrogen (theoretically up to 19.6 mass%). It is generally proposed that through thermolysis hydrogen is released from AB via a multistep

Q. Lai, Prof. K.-F. Aguey-Zinsou
MERLin
School of Chemical Engineering
The University of New South Wales
Sydney, NSW 2052, Australia
E-mail: f.aguey@unsw.edu.au
Dr. A. Rawal
NMR Facility
Mark Wainwright Analytical Centre
The University of New South Wales
Sydney, NSW 2052, Australia
The ORCID identification number(s) for the author(s) of this article can be found under https://doi.org/10.1002/adsu.201700122.

DOI: 10.1002/adsu.201700122

Dr. Md Z. Quadir
Microscopy & Microanalysis Facility
John de Laeter Centre
Curtin University
WA 6102, Australia
Dr. C. Cazorla
School of Materials Science and Engineering and Integrated Materials Design Centre
The University of New South Wales
Sydney, NSW 2052, Australia
Prof. U. B. Demirci
IEM (Institut Européen des Membranes)
UMR 5635 CNRS-ENSCM-UM
Université de Montpellier
Place Eugene Bataillon, F-34095 Montpellier, France

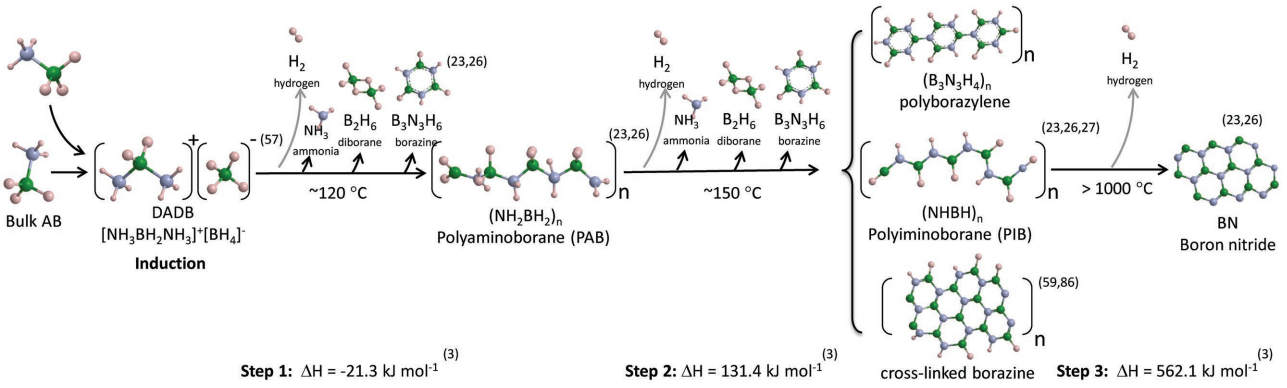

Scheme 1. Commonly accepted decomposition path of ammonia borane.[3,23,26,27,57,59,86] The first step corresponds to an induction period leading to the formation of DADB as an initiator of the polymerization process.[57] Polyiminoborane, polyborazylene and cross-linked borazine may form in various amounts depending on the decomposition process.[5,86]

process leading to the production of polyaminoborane ($(NH_2BH_2)_n$, PAB), followed by polyiminoborane ($(NHBH)_n$, PIB), and finally boron nitride $(BN)_n$ (**Scheme 1**). In this simplified pathway, each step is accompanied by the evolution of 1 equivalent of H_2.[22–24] When compared to hydrolysis, the thermolysis route is a priori much more complex owing to the compositional mixture of the solid residues obtained upon partial hydrogen release.[5] AB thermolysis also suffers from significant drawbacks including a relatively high desorption temperature (Scheme 1), and more importantly the formation of a significant amount of volatile substances contaminating the hydrogen released and leading to irreversibility. Furthermore, complete hydrogen release can only occur above 1000 °C (Scheme 1) and the final product, BN, is highly stable ($\Delta_f H = -447.69$ kJ mol^{-1}).[5] Accordingly, full release of 19.6 mass% of hydrogen from AB (3 equivalents of H_2) via the thermolysis route is considered unpractical and if reversible hydrogen paths upon hydrogen release were feasible, these should proceed away from the full decomposition of AB into BN. Hence in the best case, the release of 13 ± 1 mass% of hydrogen (2 equivalents of H_2) might be expected, which is still a high storage capacity.

Hydrogen desorption from AB is also sensitive to the decomposition conditions including, pressure, atmosphere, and heating rate, which further influence the type and amount of by-products formed including ammonia (NH_3), diborane (B_2H_6), borazine $(BHNH)_3$, cycloborazanes, diammoniate of diborane (DADB, $[(NH_3)_2BH_2]^+[BH_4]^-$) and their contribution to the overall polymerization process of AB during thermolysis (Scheme 1).[24–28] Ammonia, borazine, and diborane can poison the catalysts of proton exchange membrane (PEM) and thus are harmful to PEM fuel cells operation.[2,4,29] In addition, the melting of AB at 110 °C before hydrogen release and subsequent foaming owing to the large amount of volatiles released leads to complications in terms of practical design of AB based hydrogen storage systems. It was reported that AB can be fully desorbed at temperatures below 100 °C at a low heating rate (0.05 °C min^{-1}) without the formation of unwanted gaseous products;[26] however, this is unpractical.

To overcome these drawbacks, nanoconfinement in scaffolds, such as SBA-15,[1] carbon cryogel,[30] CMK-3,[31] MOFs,[10,32,33] and PPy nanotubes[34] have been investigated and these approaches showed improved hydrogen desorption profiles with the elimination of volatile impurities. From these findings, it is believed that a reduction of AB particle size leads a disordered phase inducing altered decomposition paths and thus lower hydrogen desorption temperatures and improved hydrogen purity owing to reduced paths for $H^{\delta+}\cdots H^{\delta-}$ intermolecular interaction, mass transfer and hydrogen diffusion.[35] Hence, confinement of AB in SBA-15 (pore size of 7.5 nm) showed a hydrogen peak at 98 °C,[1] whereas for confinement in carbon cryogel with a pore size <5 nm led to further reduction of the hydrogen desorption temperature with a peak at 85 °C.[30] The wall of these scaffolds were also claimed to provide additional nucleation sites facilitating the dehydrogenation of AB. The approach of destabilization with reactive hydrides such as LiH,[8] or metal halides (e.g., Co and Ni)[9,34,36–38] has also been explored and some decrease in desorption temperatures has been achieved, but to date no direct reversibility of the hydrogen release has been observed.

Taking into account these recent findings, herein we investigated an alternative route, whereby we aimed at confining ammonia borane within a nanosized nickel matrix in order to utilize nanoconfinement and nickel (Ni) catalytic effect[9,36] to suppress the melting of AB, hinder the formation of volatile by-products and establish a direct path for the regeneration of the amino borane compound from hydrogen pressure only. Computational studies have predicted that the enthalpy for decomposition of AB to form polymeric compounds are between −13.3 and 38.4 kJ mol^{-1},[4,39,40] meaning that some of these compounds could potentially be rehydrogenated back to ammonia borane or an intermediate form under mild conditions of temperature and pressure.[5] Our study reveals that this is the case when Ni and AB are intimately combined at the nanoscale.

2. Results and Discussion

2.1. Synthesis of Ammonia Borane Nanoparticles and Hydrogen Properties

Commercial ammonia borane complex (Bulk-AB) consisted of large particles with sizes >1 μm as shown by scanning electron

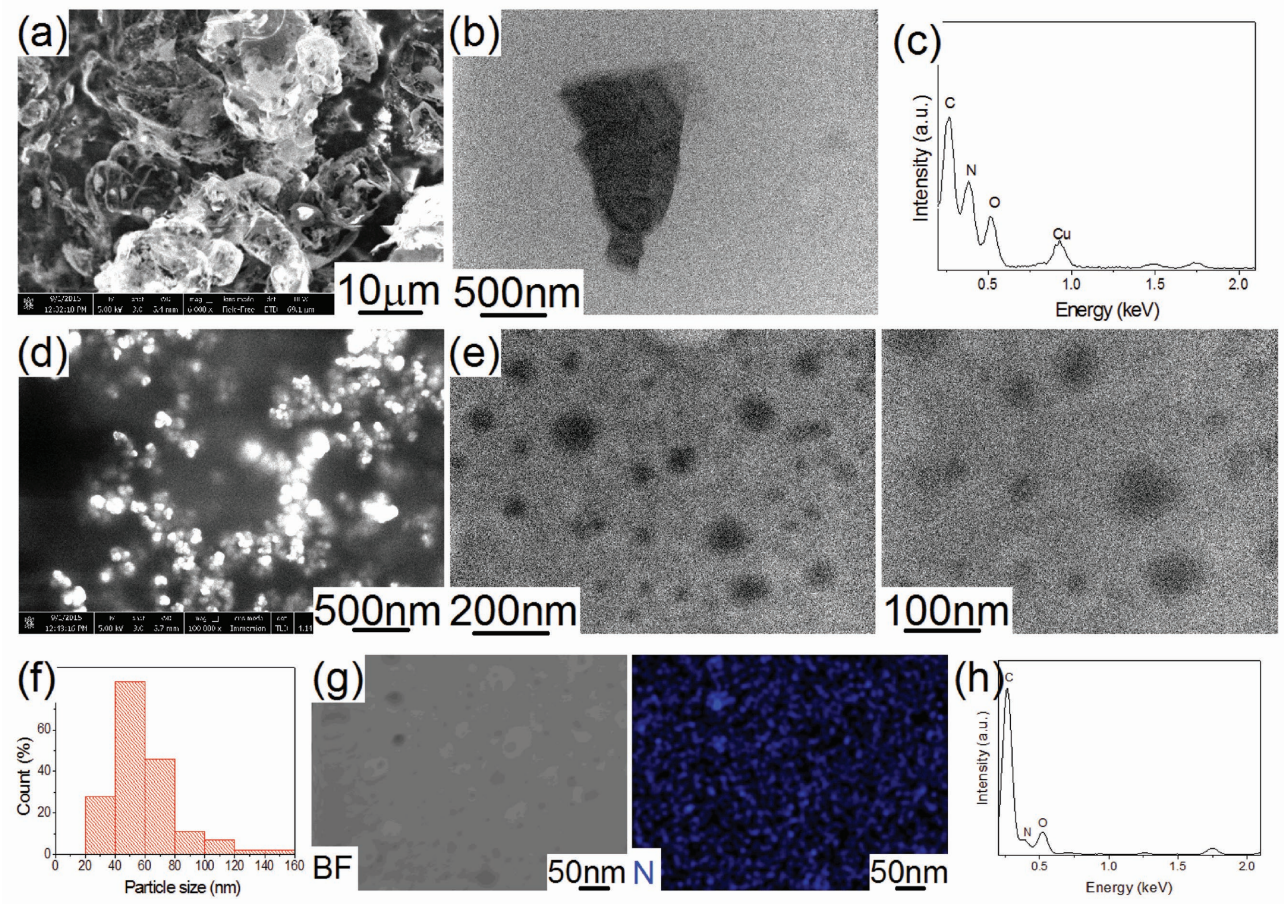

Figure 1. a) SEM and b) TEM images of Bulk-AB as received with c) corresponding EDS signal. d) SEM and e) TEM images of Nano-AB as-synthesized with corresponding f) particles size distribution, g) EDS elemental mapping for nitrogen (N), and h) associated EDS analysis.

microscopy (SEM) and transmission electron microscopy (TEM) (**Figure 1**a,b). In contrast, by using an antisolvent precipitation method with oleic acid as a surfactant stabilizing the formation of isolated AB particles, nanosized AB (Nano-AB) was synthesized with a particle size ranging from 20 to 160 nm (Figure 1d–f). Energy dispersive X-ray spectroscopy (EDS) confirmed the nitrogen content in Bulk-AB as well as in Nano-AB and this proved that the particles observed effectively corresponded to AB (Figure 1c,h). This was further confirmed by elemental mapping (Figure 1g). Hence, the approach of antisolvent precipitation, whereby a saturated solution of AB is precipitated in a solvent where AB is not soluble was effective in generating AB nanoparticles. X-ray diffraction (XRD) of Nano-AB confirmed the crystalline nature of the material along the known tetragonal phase (Figure S1, Supporting Information). However, a split of the major peak at 23.9° (110) and 24.4° (101) was observed in Nano-AB. Such a behavior, akin to the observations of AB encapsulated in carbon cryogel,[30] has previously been assigned to the stress exerted on the AB crystal by the carbon matrix. Considering that the head of the oleic acid surfactant (a carboxylic group) may strongly bind to the surface of the AB particles, owing to the favorable substitution of H in B—H and N—H by oxygen bonds, a dense network of surfactants at the surface of AB may exert some localized stress. Scherrer analysis of the diffraction pattern showed a significant reduction of the crystalline size to 42 ± 2 nm for Nano-AB as compared to 78 ± 2 nm for Bulk-AB and this is in agreement with the TEM observations in Figure 1. FTIR analysis (Figure S2, Supporting Information) also confirmed the vibrations that were assigned to N—H and B—H stretching and bending modes in agreement with the spectral signature of Bulk-AB.[41] The additional C—H vibration at 2750 cm^{-1}, only visible on the FTIR spectrum of Nano-AB, confirmed its stabilization with oleic acid (Figure S2, Supporting Information).

To determine the effect of particle size on the hydrogen desorption properties of ammonia borane, the bulk and nanoparticles were characterized by thermogravimetric analysis (TGA)/differential scanning calorimetry (DSC)/mass spectrometry (MS). The thermal decomposition profile of unmodified AB was in agreement with previous investigations (**Figure 2**a).[23,24,42] Concomitant with the melting of AB at 112 °C, hydrogen was released between 100 and 175 °C as observed by MS. The subsequent three exothermic peaks (118, 124, 160 °C) as revealed by DSC were attributed to the multistep and complex decomposition process of AB.[3,22,23,41] TGA showed two major mass losses of 25 and 44.4 mass%, which are significantly larger than the theoretical hydrogen content of AB and the amount of hydrogen that should be released following

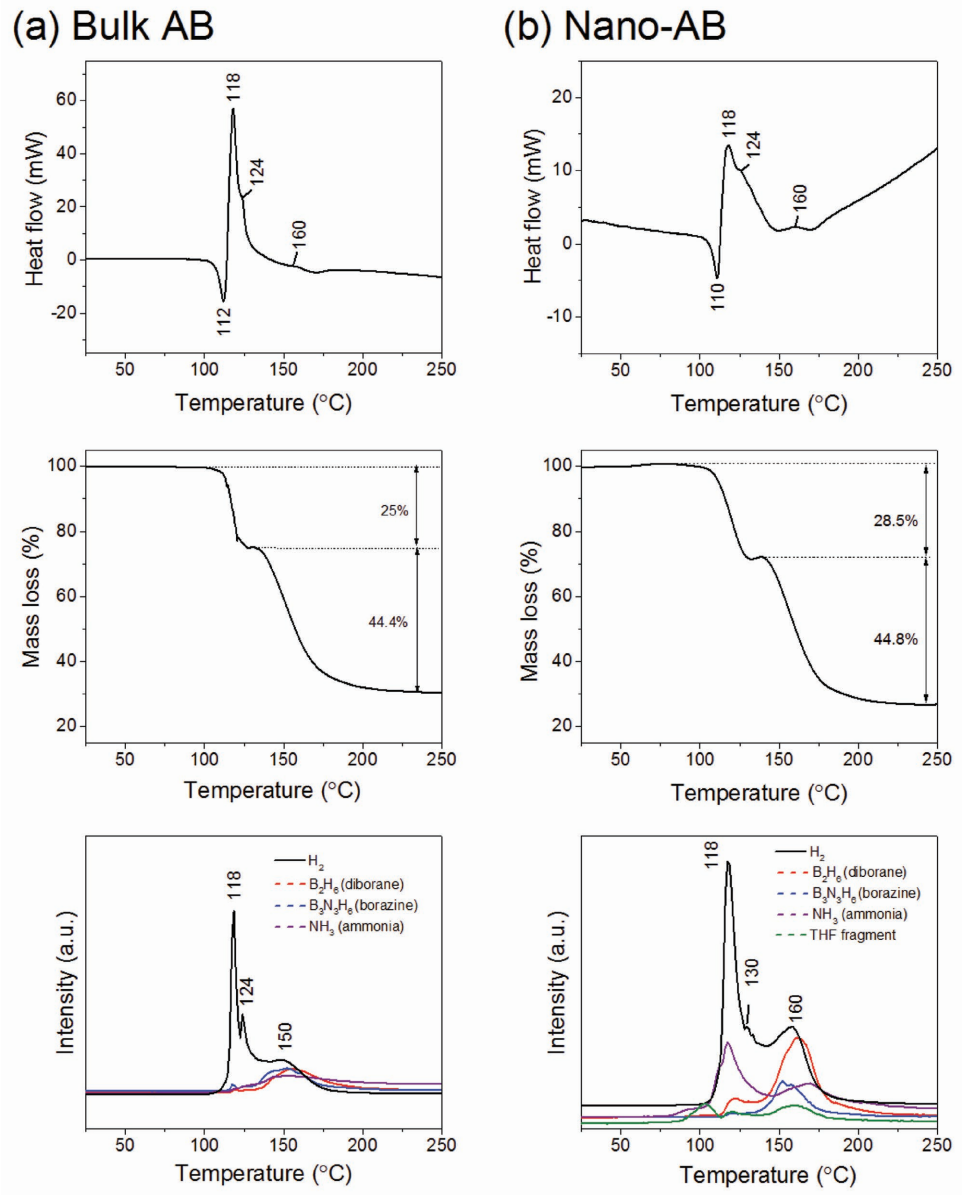

Figure 2. Thermal decomposition of a) Bulk-AB as received and b) Nano-AB as-synthesized, monitored by TGA/DSC/MS at a heating rate of 10 °C·min^{-1} under a Ar flow of 20 mL min^{-1}. Fragments assigned to THF were also observed owing to remaining traces of THF bonded to Nano-AB. No decomposition of oleic acid was observed within this temperature range. As per Figure S3 in the Supporting Information oleic acid decomposes at temperatures >200 °C and once stabilizing a nanoparticle higher decomposition temperatures have been reported.[87]

steps 1 and 2 (Scheme 1), i.e., ≈13 mass%. This suggested the formation of gaseous by-products including borazine, diborane, and ammonia which was also observed by MS as per previous reports.[3–5]

Nano-AB exhibited a similar hydrogen desorption profile (Figure 2b). Hydrogen was released in multiple steps between 100 and 175 °C, with corresponding exothermic peaks observed by DSC. Even though the stabilization of AB nanoparticles with oleic acid showed no significant improvement in the temperature for hydrogen release, it demonstrates the potential of the nanozing approach adopted owing to the significant reduction of foaming (**Figure 3**a). The decrease in foaming may indicate some modifications in the decomposition path of AB upon nanozing and surfactant stabilization as reflected by the larger amount of ammonia detected by MS at the very beginning of the melting of Nano-AB (Figure 2b). The later was attributed to the reduction of the oleic acid head group by the BH_3 moieties[43] at the surface of the AB nanoparticles. However, the surfactant was clearly unable to contain the melting of AB, and thus facilitate a more controlled release of hydrogen through the effective confinement of the melt. Indeed, further TEM analysis of Nano-AB along its decomposition path indicated significant morphological degradation and the loss of the spherical shape of the Nano-AB particles upon melting and agglomeration (Figure 3b–d).

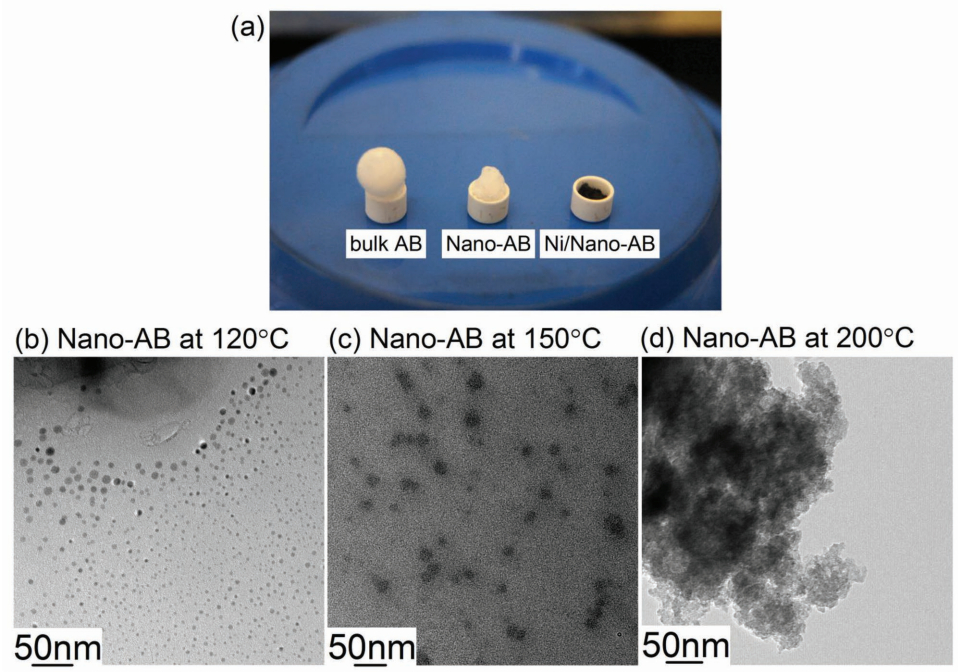

Figure 3. Images of a) Bulk-AB, Nano-AB, and Ni-Nano-AB after thermal decomposition at 250 °C at 10 °C·min^{-1} under constant Ar flow of 20 mL min^{-1}; and bight field TEM images of Nano-AB heated at 10 °C·min^{-1} under constant Ar flow of 20 mL min^{-1}, up to a) 120 °C, b) 150 °C, and c) 200 °C.

A better method is thus required to effectively stabilize the AB nanoparticles and fully contain the decomposition products so inter and intramolecular reactivity of $H^{\delta+}\cdots H^{\delta-}$ can be enhanced to limit the amount of side products generated and keep the decomposition products in close vicinity to potentially enable reversibility. As per previous investigations this can be achieved to some extent by confining AB within the porosity of a host inorganic material.[1,30,32,34] However, this approach brings significant limitations in terms of (i) achieving high hydrogen storage capacity owing to the difficulty of fully filling the porosity and (ii) reversibility because the open porosity possibly leads to a loss of confinement in addition to a partial reaction of AB with the host matrix.[35] Accordingly to date no reversibility has been achieved through the nanoconfinement of AB in host porous matrixes. However, the hydrogenation of iminoborane (HNBH) to aminoborane ($H_2N{-}BH_2$) has been predicted to be exothermic (–131.4 kJ mol^{-1});[3,44] hence it may be possible to rehydrogenate iminoborane type compounds under mild conditions of pressure and temperature, while the hydrogenation of aminoborane to ammonia borane is endothermic (21.3 kJ mol^{-1}).[39] Polymeric aminoborane however decomposes through an exothermic process,[27] hence the thermal decomposition of Bulk-AB and subsequent hydrogen and by-products generation leading to large polymeric aminoborane chains is unlikely to lead to reversibility[45] unless polymeric growth is significantly limited. Such a chain growth can be limited through the full confinement of nanosized AB particles within a closed shell and/or an assisted catalytic process. Full confinement of nanosized AB could be achieved through the strategy of a core–shell approach previously developed for $NaBH_4$,[46] whereby the $NaBH_4$ nano-core is contained within the metallic shell of a transitional metal with "good" hydrogen properties in terms of hydrogen activation, diffusion and permeability.[47] Partial polymerization of AB has also been observed upon the reduction of metal halides by pristine AB.[48–50] Hence, the combination of both approaches was investigated.

2.2. Modification of Nano-AB with Ni

To stabilize the nanoparticles of AB, nickel (Ni) was chosen due to its good hydrogen properties in terms of permeability, diffusivity[51] and known catalytic effect on both hydrolysis[19] and thermolysis[36] of AB. Ni^{2+}/Ni has a mild redox potential (E = –0.257 V vs NHE) and thus it can be readily reduced by AB (E = –1.21 V vs NHE).[37] Accordingly, a simple way to coat the surface of the AB nanoparticles with Ni is to adapt the methods developed for the synthesis of inorganic core–shell structures, and in particular transmetalation methods involving the formation of a stable shell through a chemical reaction between the shell and the core.[52,53] In the transmetalation method, a metallic shell is formed by the reduction of a metal salt at the surface of a core initially synthesized. As the metal salt is reduced and deposited at the surface of the core, the reaction products diffuse through the shell layer into the bulk solution leading to a homogenous growth of the shell. Based on these principles, the reducing property of the BH moieties in AB could be similarly used to form Ni coated AB. However in this process, the growth of the Ni layer is difficult to control owning to the large difference in reduction potential of AB and $NiCl_2$, the Ni/AB lattice mismatch and high interfacial energy[54,55] favoring fast Ni deposition and thus dendritic and heterogeneous Ni growth in lieu of the formation of a continuous Ni layer at the surface of AB. To moderate this, the approach was

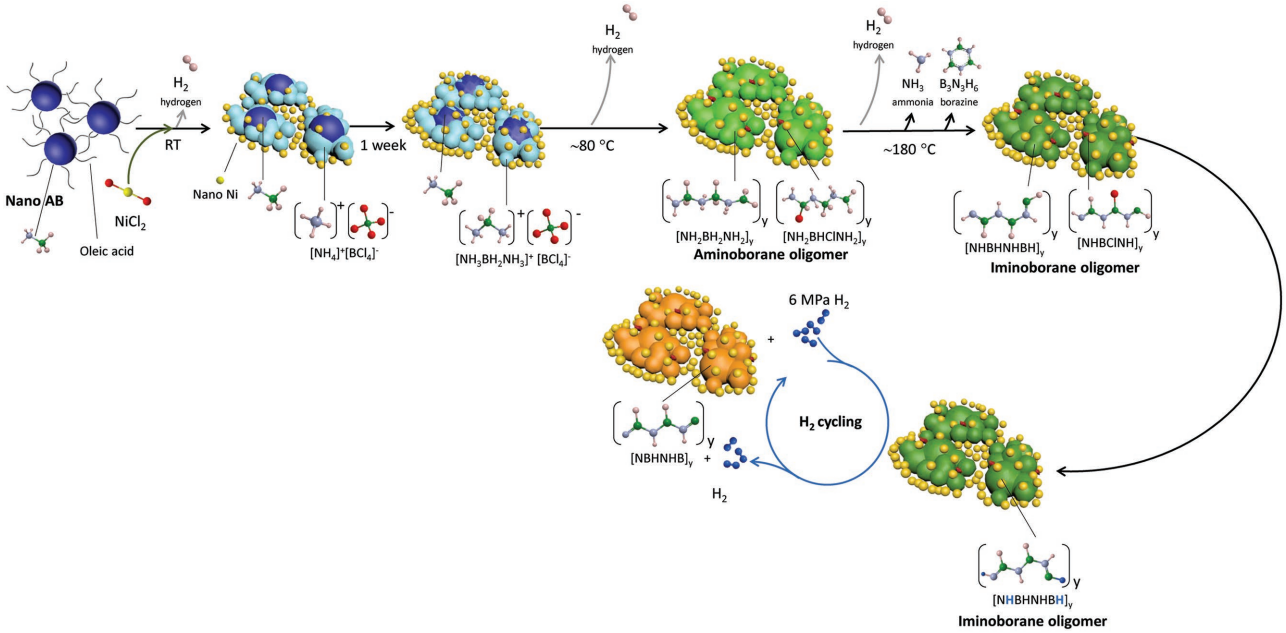

Scheme 2. Synthetic and decomposition path of Ni/Nano-AB leading to hydrogen reversibility. Upon nanosizing and $NiCl_2$ reduction the formation of $[NH_4]^+[BCl_4]^-$ is assumed to initiate the oligomerization of AB and the resulting Ni matrix to limit chain growth. (*y*) corresponds to the oligomeric chain length.

thus to carry the reduction of $NiCl_2$ at the surface of the Nano-AB particles through a solid state reaction involving the formation of $[NH_4]^+[BCl_4]^-$ and Ni^0 (reaction 2).[49,56] This would also lead to a partial oligomerization of AB[48–50] (reaction 3) following a mechanism akin to that reported for the polymerization of AB through its reaction with DADB during thermal decomposition.[3,57] However here, $[NH_4]^+[BCl_4]^-$ formed upon the first reduction of $NiCl_2$ would facilitate the formation of dimeric, and eventually short oligomeric products owing to limited ionic diffusion in such a solid state reaction (**Scheme 2**)

$$2NiCl_2 + H_3NBH_3 \rightarrow [NH_4]^+[BCl_4]^- + H_2 + 2Ni \quad (2)$$

$$[NH_4]^+[BCl_4]^- + H_3NBH_3 \rightarrow [H_3NBH_2 - NH_3]^+[BCl_4]^- + H_2 \quad (3)$$

$NiCl_2$ powder was thus mixed with Nano-AB and stirred at a controlled rate. After reaction over a week, the color of the mixture (denoted Ni/Nano-AB) turned from gray to black indicating the formation of metallic nickel.

After reaction, FTIR analysis confirmed that Ni/Nano-AB still displayed vibrations corresponding to the main AB phase (Figure S2, Supporting Information). TEM analysis of Ni/Nano-AB showed isolated nanoparticles with sizes ranging from 1 to 7 nm (**Figure 4**a–c). EDS analysis further confirmed the B, N, and Ni contents of the particles imaged (Figure 4d). However, in dark-field mode these nanoparticles appeared to be mostly bright, suggesting that the darker particles observed in bright field (BF) (Figure 4a–c) were mainly Ni nanoparticles (Figure 4e). This was confirmed by elemental mapping showing Ni agglomerates evenly distributed across the N and B signals (Figure 4e). Hence, it is apparent that the solid state approach of $NiCl_2$ reduction at the surface of nanosized AB led to a degradation of the initial spherical morphology of Nano-AB. This was explained by the oligomerization of AB (reaction 3) as evidenced by the appearance of an additional amorphous disordered phase in solid state ^{11}B nuclear magnetic resonance (NMR) spectrum of Ni/Nano-AB (Figure S4a,b, Supporting Information). As per previous reports, Bulk-AB showed two signals centered at about −24 ppm, due to quadrupolar coupling (Figure S4a, Supporting Information).[58] The sharpness of the peaks suggested high crystallinity.[58] However, as-synthesized Ni/Nano-AB exhibited two distinct sites that were assigned to an amorphous and crystalline H_3BNH_3 domains.[57] XRD analysis also confirmed a partial oligomerization of Nano-AB upon reaction with $NiCl_2$ (**Figure 5**). In addition to peaks related to the tetragonal ammonia borane phase and metallic Ni, new diffraction peaks in the range 12– 22° were observed and assigned to oligo/polymeric forms of $(BH_2NH_2)_n$ and $(BH_xNH_x)_n$ (with $x < 2$) as per previous reports.[41,59,60] The oligomerization of AB upon reaction with $NiCl_2$ via the formation of the intermediate $[NH_4]^+[BCl_4]^-$ was also confirmed by X-ray photoelectron spectroscopy (XPS) analysis of Ni/Nano-AB as-synthesized (Figure S5b,d, Supporting Information). Indeed, in comparison to Bulk-AB (Figure S5d, Supporting Information), the N(1s) spectrum of Ni/Nano-AB displayed in addition to the peak at 400.28 eV corresponding to N—H bonds in H_3BNH_3,[61] a peak with a binding energy of 401.70 eV which is related to N—H in NH_4^+ (Figure S5b, Supporting Information).[62,63]

Selected area electron diffraction (SAED) also corroborated the crystalline nature of the nanoparticles observed with diffraction planes corresponding to that of tetragonal AB and cubic ($Fm3m$) Ni in agreement with the XRD results (Figures 4f and 5). The metallic nature of Ni was also validated by XPS analysis (Figure S6, Supporting Information). Hence,

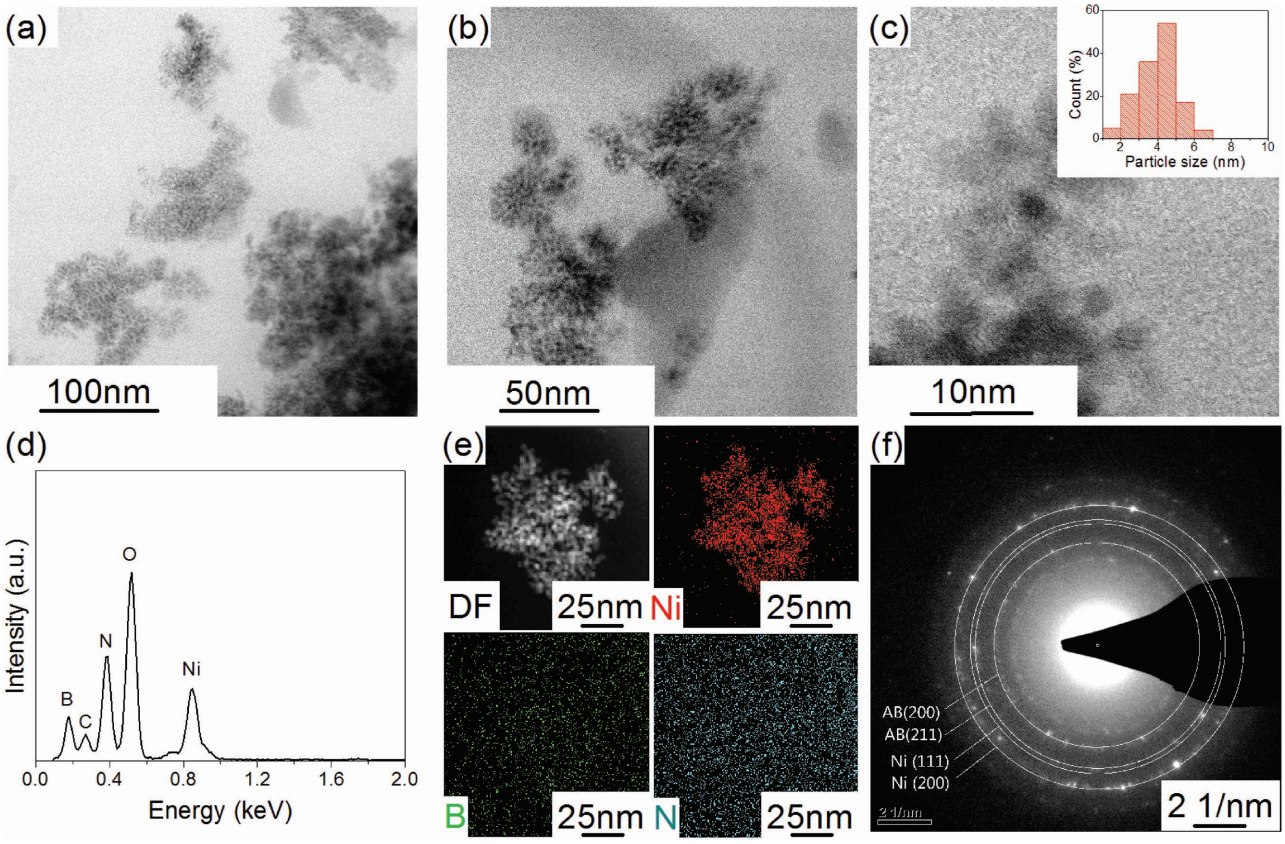

Figure 4. STEM images of Ni/Nano-AB as-synthesized a–c) in bright-filed mode, d) corresponding EDS analysis, e) associated dark-filed image and elemental mapping of Ni, B, and N and f) SAED pattern shows the presence of AB and Ni phases. The insert in (c) corresponds to the Ni particle size distribution measured from several bright field images.

considering the high level of Ni nanoparticles distribution across the material, it is believed that the reduction of $NiCl_2$ with AB led to AB nanodomains embedded within a matrix of oligomeric $(BH_xNH_x)_y$ (with y corresponding to the chain length) and nanosized Ni. It is noteworthy that reduction of $NiCl_2$ with Bulk-AB also occurs. However, as exemplified by XRD analysis and the smaller diffraction peaks corresponding to a oligo/polymeric from $(BH_xNH_x)_n$ (Figure 5), this reaction is slower at room temperature than with Nano-AB.

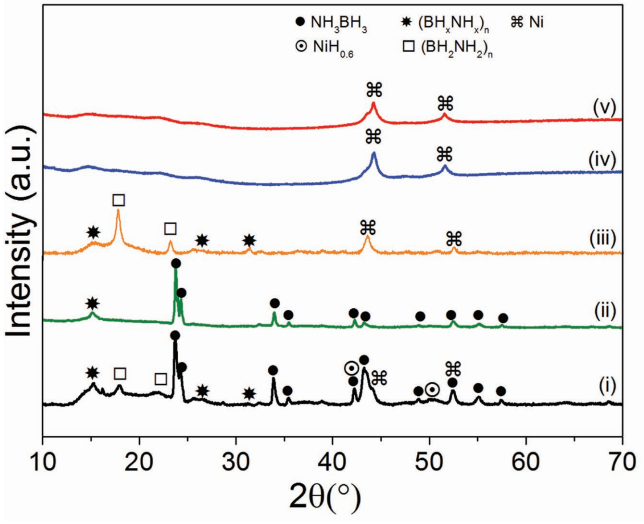

Figure 5. XRD patterns of i) Ni/Nano-AB as-synthesized, ii) Bulk-AB mixed with 45 wt% of $NiCl_2$ as a reference, and Ni/Nano-AB after iii) heat treatment at 75 °C over 24 h and under 6 MPa hydrogen pressure to slow the decomposition, iv) after hydrogen cycling at 350 °C in the absorbed, and v) desorbed state.

2.3. Hydrogen Desorption Properties of Ni/Nano-AB and Reversibility

Ni/Nano-AB started to release hydrogen as low as 50 °C, i.e., 50 °C lower than the bulk, and hydrogen desorption still followed a multistep decomposition process as for Nano and Bulk-AB (**Figure 6**a). However, the release of ammonia, diborane, and borazine was significantly reduced with only pure hydrogen up to 100 °C and then a small and continuous release of ammonia followed by some traces of borazine from 200 °C (Figure 6b). Below 100 °C, Ni/Nano-AB starts to polymerize toward polyaminoborane, i.e., $(H_2BNH_2)_n$, as proven by the XRD and FTIR of the material left at 75 °C over 24 h (Figure 5 and **Figure 7**). Hence, the clean release of hydrogen observed at low temperatures should be the result of additional self-recombination of oligomeric entities resulting from the initial $NiCl_2$ reduction process and their reaction

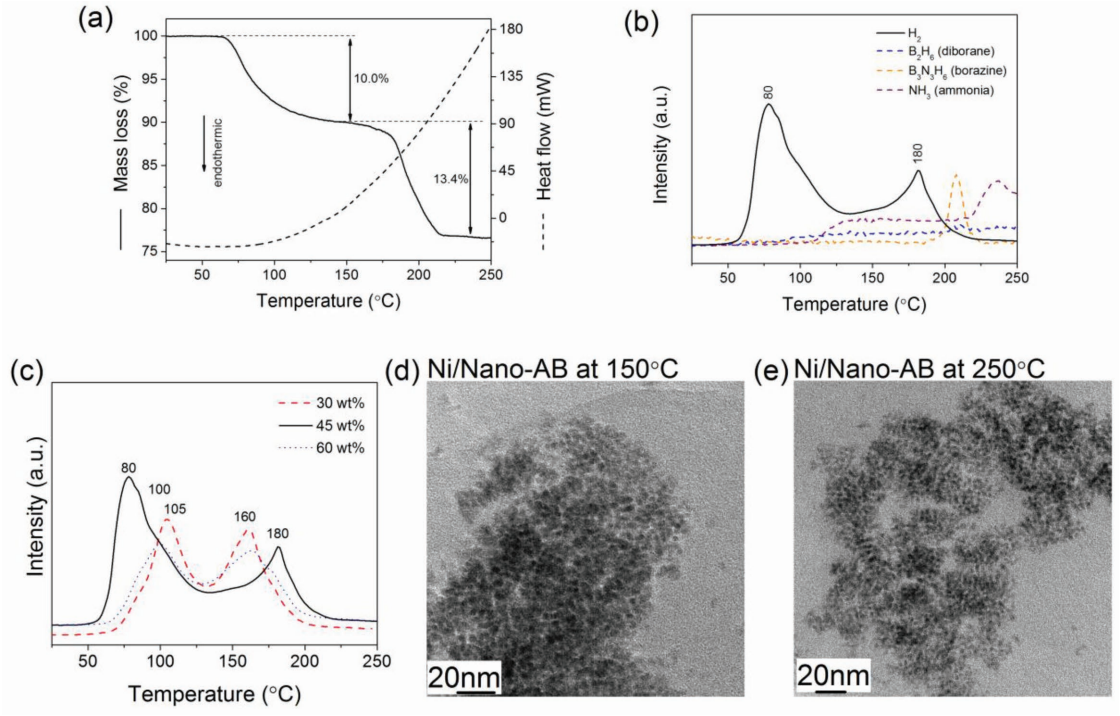

Figure 6. Thermal decomposition of a) Ni/Nano-AB as-synthesized with 45 wt% of $NiCl_2$ at a heating rate of 10 °C·min^{-1} under a Ar flow of 20 mL min^{-1}, and b) associated hydrogen desorption profile followed by MS. Fragments associated with B_2H_6, $B_3N_3H_6$, and NH_3 were also observed above 100 °C. c) Effect of the amount of $NiCl_2$ on the hydrogen desorption profile of Nano-AB, and bright field TEM images showing the evolution of the Ni nanoparticles morphology in Ni/Nano-AB with 45 wt% of $NiCl_2$ after its thermal decomposition at d) 150 °C and e) 250 °C.

with additional H_3BNH_3 to lead to longer oligomeric entities (Scheme 2).[48] At temperatures above 100 °C, further decomposition of remaining $[NH_4]^+[BCl_4]^-$ or $[H_3NBH_2–NH_3]^+[BCl_4]^-$ type compounds into H_3NClBH_2 would release traces of ammonia as observed by MS (Figure 6b). Once these are consumed, it is possible that the initial decomposition process of Ni/Nano-AB will follow to some extent that reported for polyaminoborane[27,59] with the loss of NH_x and BH_x fragments ($x \leq 3$) and subsequent release of some borazine upon recombination of these fragments at temperatures >200 °C (Scheme 2 and Figure 6b).[64] Assuming a decomposition path akin to that reported for Bulk-AB, at the end of the decomposition process a polyiminoborane and/or polyborazylene type structure should remain.[5,41,59]

Ni/Nano-AB after thermal decomposition remained black without apparent foaming and thus excessive liberation of volatiles (Figure 3a). Indeed, the DSC signal showed no major endothermic or exothermic events as observed for Bulk and Nano-AB (Figures 2a,b and 6a). This could indicate a different decomposition path with the suppression of the melting of AB. The TGA curve (Figure 6a) showed 10% and 13.4% mass loss for the two main hydrogen release steps, which is higher than the theoretical hydrogen content of 12.0 mass%, including the Ni content. Once again, the excess mass loss is related to the additional production of ammonia and borazine during the thermal decomposition of Ni/Nano-AB. However, this is significantly lower than the mass loss of >69% observed for Bulk and Nano-AB (Figure 2). Bulk-AB mixed with $NiCl_2$ in a similar manner also displays a higher mass loss of 36.9% (Figure S7, Supporting Information); but more remarkably, its decomposition is still occurring through a melting transition and its hydrogen release profile, although starting at a lower temperature of 60 °C, remains similar to that of unmodified Bulk-AB. It is thus apparent that a nanosize approach leads to lower starting desorption temperatures but also less side products as a result of short diffusion paths and a close vicinity of the reactants. In order to further reduce the starting temperature for hydrogen release, varying amounts of $NiCl_2$ were also investigated but it appeared that the original amount of 45 wt% of $NiCl_2$ was leading to the lowest temperature for the initial release of hydrogen (Figure 6c). Through the thermal decomposition of Ni/Nano-AB, the Ni nanoparticles did not sintered and their morphology did not evolve. This further corroborated the hypothesis that Ni was forming with AB a relativity well defined matrix (Figure 6d,e).

Investigations on the reversibility of Ni/Nano-AB were first carried out at 350 °C, after all the major hydrogen desorption events and at a temperature significantly below the conversion of polymeric $(BH_xNH_x)_n$ into BN (Scheme 1).[41] At 350 °C and 6 MPa H_2 pressure, a stable 1 mass% hydrogen capacity was achieved (**Figure 8**a). Measurement of the hydrogen kinetics showed that the absorption was very fast and all hydrogen was absorbed within the first 50 min. However, the hydrogen desorption process was relatively slow in comparison, with full release occurring after 250 min.

Further analysis of the rehydrogenated material with TGA (Figure 8b) also showed around 1% of mass loss under flowing Ar and full hydrogen release was achieved at

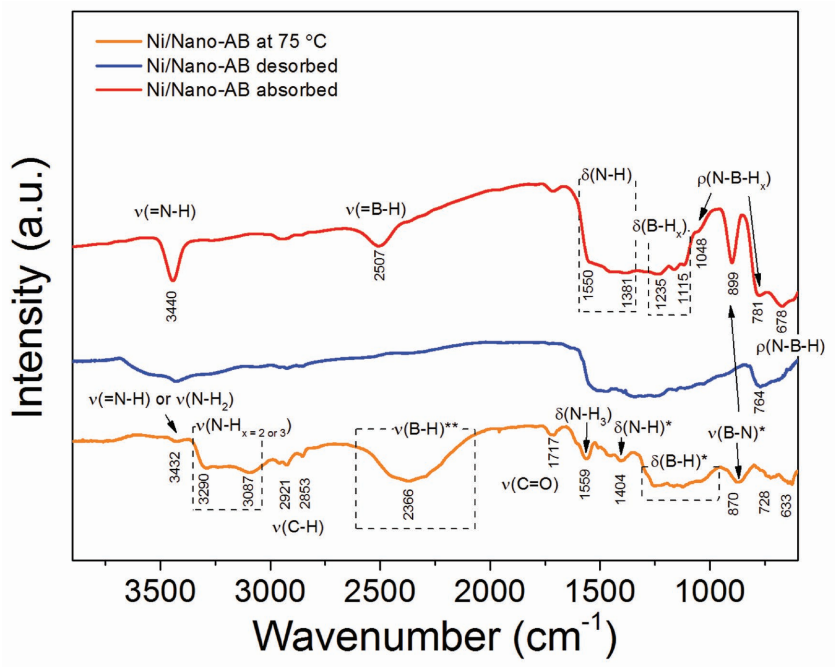

Figure 7. FTIR spectra of Ni/Nano-AB after heat treatment at 75 °C for 24 h under 6 MPa hydrogen pressure, and after hydrogen cycling at 350 °C in the desorbed, and absorbed state. The apparition of the band at 3432 cm^{-1} at 75 °C indicates the formation of a oligomeric $(HN{=}BH)_y$ type structure or terminal NH_2 groups in a oligomeric aminoborane structure. ν(B—H)** may involve BH_3 and BH_2 vibrations. The vibration δ(N—H)* is assigned to the umbrella vibration mode of the terminal NH_3 group. The vibration ν(B—N)* corresponds to the respective BN stretching vibration involving the terminal NH_x group ($x \leq 3$), and δ(B—H)* possibly involves unresolved bending modes including BH_2 deformation and BH_3 umbrella.[41] The C—H and C=O vibrations correspond to that of oleic acid.[88]

250 °C which is below the 350 °C needed through cycling (Figure 8a). This would indicate that hydrogen desorption from this material is sensitive to the residual hydrogen partial pressure, hence the slow hydrogen desorption kinetics observed under a 0.01 MPa hydrogen pressure. To verify this, the material was reabsorbed on a homemade Sievert apparatus at a lower temperature of 200 °C, i.e., just after hydrogen release from Ni/Nano-AB (Figure 6b). Once again upon heating under Ar flow, the material showed reversibility with hydrogen release occurring before 250 °C (Figure S8, Supporting Information), which further confirmed the ability of the Ni/Nano-AB material to reversibly store hydrogen under mild conditions of temperature and pressure. More remarkably, reversible hydrogen release occurred with no detectable impurities (Figure 8c). Release of common impurities such as diborane, borazine, and ammonia found during the thermal decomposition of AB was totally suppressed; and thus once Ni/Nano-AB is desorbed a first time, only hydrogen is cycled. To confirm reversibility, XRD analysis was carried out but no diffraction peaks except those corresponding to Ni were observed, and this indicated the amorphous nature of the reversible material (Figure 5). However, FTIR analysis of the material clearly showed the reappearance of sharp N—H and B—H stretching vibrations upon hydrogen absorption meaning that the material could reabsorb hydrogen (Figure 7). To confirm this, solid state ^{11}B NMR analyses were also carried out. After hydrogen desorption the signal at around −24 ppm disappeared in favor of two peaks at 24 and 36 ppm (Figure S4c, Supporting Information). Following previous reports, the primary peak at 24 ppm should be assigned to B coordinated to three N (BN_3) sites in a polyborazylene type structure while the second peak at 36 ppm should correspond to the hydrogen bearing $H{-}BN_2$ sites in the same polymer.[59,65] After hydrogenation, no significant changes appeared in the spectral signature of the material, which indicated that the polymeric structure remained the same (Figure S4d, Supporting Information). However, quantification of the ^{11}B NMR spectra showed differences in ratios between the two sites. The ratio of the primary (BN_3) to secondary ($H{-}BN_2$) peak decreased from 4.5:1 (desorbed state) to 3.5:1 after hydrogenation, indicating that the adsorbed material had a higher concentration of B—H sites and therefore more hydrogen was attached to the polymer as observed by FTIR and hydrogen release/uptake measurements (Figures 7 and 8). XPS analysis also confirmed a similar trend. As shown in Figure S5 in the Supporting Information, in as-synthesized Ni/Nano-AB components of the B(1s) spectrum corresponded to that of Bulk-AB with binding energies at 190.01 and 188.40 eV related to B—N and B—H bonds in the H_3BNH_3 structure,[66] respectively. Upon hydrogen absorption and desorption, the binding energy related to B—N in as-synthesized Ni/Nano-AB shifted from 190.01 eV to slightly higher values of 190.63 and 190.61 eV, respectively, and this was consistent with a oligo/polymeric $(BH_xNH_x)_n$ structure.[60] Similarly, the N(1s) spectrum of Ni/Nano-AB in the absorbed and desorbed states displayed peaks at ≈399.24 eV corresponding to N—H bonds in a $(BH_xNH_x)_n$ polymer,[60] and a peak at 399.54 eV assigned to terminal N—H bonds in that polymeric structure.[67] It is noteworthy that no shift was observed in the N(1s) spectrum of Ni/Nano-AB upon hydrogen absorption/desorption but the $(N{-}H)_n/N{-}H$ peak ratio increased by a factor 1.6 upon hydrogen absorption (Table S1, Supporting Information) meaning that the polymeric structure is carrying more hydrogen in its absorbed state as compared to the desorbed state. Hence, it is apparent that upon a first decomposition and release of hydrogen up to 350 °C, Ni/Nano-AB can reversibly store hydrogen with some hydrogen reversibly binding to nitrogen and boron sites.

TEM analysis of Ni/Nano-AB after cycling did not show significant evolutions in morphology (Figure 8d). Bright-field images showed dark nanoparticles corresponding to Ni with a particle size ranging from 1 to 7 nm. In dark-field modes, these dark particles appeared to be bright, indicating metallic Ni nanoparticles and elemental mapping further validated

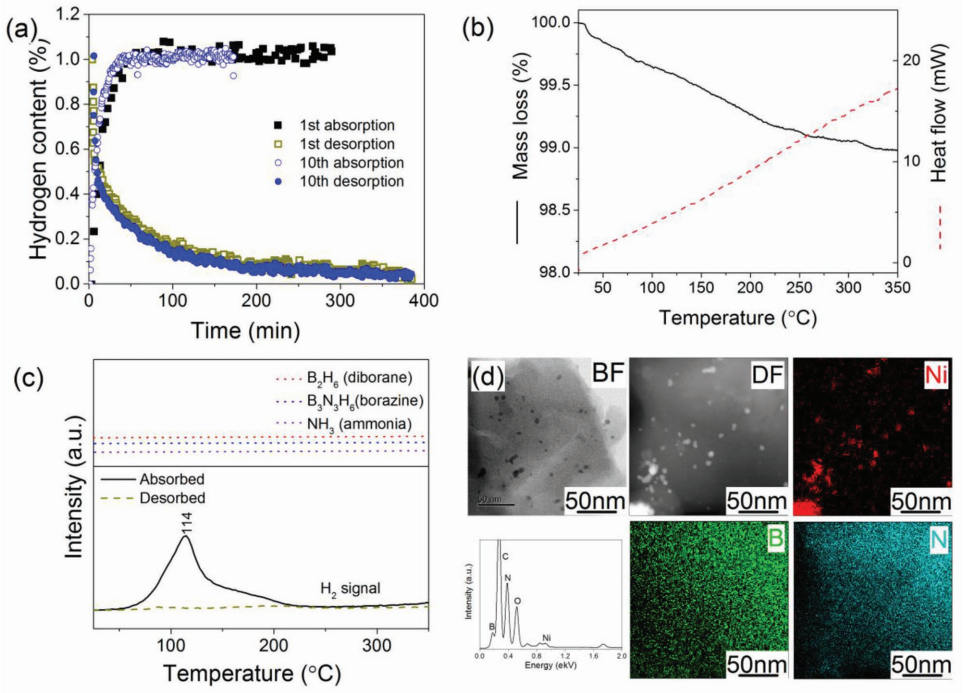

Figure 8. a) Kinetics of hydrogen desorption at 0.01 MPa and absorption under 6 MPa hydrogen pressure at 350 °C of Ni/Nano-AB—The hydrogen capacity corresponds to that of the entire composite material. Thermal decomposition profile of Ni/Nano-AB in the absorbed state after cycling as characterized by b) TGA/DSC and c) MS. Except hydrogen no other gases were detected by MS. Ni/Nano-AB in the desorbed state releases no hydrogen. d) TEM images of Ni/Nano-AB after hydrogen cycling at 350 °C in bright-field and dark-field mode and corresponding EDS analysis and elemental mapping of Ni, B, and N.

the high dispersion of these Ni nanoparticles among the $(BH_xNH_x)_n$ polymer.

2.4. Nature of the Improvement

To evaluate if the reversibility observed was purely due to the reaction of AB with $NiCl_2$, hydrogen reversibility was investigated for Bulk-AB reacted with 45 wt% of $NiCl_2$ (Ni/Bulk-AB). As shown by XRD, the reaction of Bulk-AB with $NiCl_2$ also leads to a partial polymerization of AB (Figure 5); and this is confirmed to some extent by FTIR analysis showing weaker vibrational peaks indicating some level of disorder and thus polymerization (Figure S9, Supporting Information).[42] However, the thermal decomposition of Ni/Bulk-AB still leads to melting of AB and significant release of impurities in addition to hydrogen (Figure S7, Supporting Information). According to XRD analysis, the end point of this desorption process at 250 °C is a polymeric structure resulting from the decomposition of AB,[59,68] with additional metallic nickel in the case of Ni/Bulk-AB (Figure S10, Supporting Information). However, this polymeric compound does not reabsorb hydrogen as proven by FTIR and thermal decomposition analysis (Figures S9 and S11, Supporting Information). It is thus apparent that the polymeric structure formed at the nanoscale through the reaction of $NiCl_2$ with Nano-AB is different to that generated with Ni/Bulk-AB through its ability to reversibly absorb hydrogen. The exact chemical structure of this polymeric structure remains unclear, but the various characterizations carried out would indicate that only some sites on the Ni/Nano-AB structure can be de/rehydrogenated owing to the low reversible hydrogen capacity achieved. It is accepted that the decomposition of AB despite its complexity leads to the formation of linear and/or cyclic polymeric structures including polyaminoborane (≈100 °C), polyiminoborane followed by polyborazylene (≈140 °C)[5,69] leading to hexagonal BN at temperatures above 1000 °C[41] (Scheme 1).

According to the NMR analysis (Figure S4, Supporting Information), it is possible that the reversible structure with a spectrum akin to that reported for polyborazine[65] will have a similar structure with BN_3 and $H{-}BN_2$ sites. Considering, this hypothesis, only terminal B and N will have the ability to reversible uptake hydrogen, hence the low storage capacity observed. XPS also indicates that this structure contains B—N bonds with binding energies away from that of AB or boron nitride but closer to that reported for B—N polymeric structures holding hydrogen bonds.[60] Furthermore, FTIR analysis of the transition between the absorbed and desorbed states shows the appearance of the relatively sharp N—H, N—B—H, and B—H stretching vibrations instead of weak and broad peaks observed upon hydrogen release, and this indicates some reordering of the polymeric structure upon hydrogen absorption (Figure 7). The vibrations at 1048 and 781 cm^{-1} appearing in the material after hydrogen absorption and assigned to N—B—H rocking confirm the uptake of hydrogen and reordering of the polymeric structure. The reappearance of the strong vibration at 899 cm^{-1} upon hydrogen absorption is also an indicator of BN stretching

mode associated with terminal NH_x groups ($x \leq 2$),[41,70] and this further supports the hypothesis that the hydrogen absorption/desorption process only occurs at specific sites at the edge of the polymeric structure and/or along pending/terminal groups. The FTIR bands at 3440 and 2507 cm^{-1} reappearing upon hydrogen absorption are also consistent with NH and BH stretching modes involving boron/nitrogen π bonds.[41] Accordingly, the polymeric structure reversibly absorbing hydrogen involves π bonds and thus is not a polyaminoborane type structure. Despites the indication from NMR of BN_3 sites, it is also not a polyborazylene type structure involving B_3N_3 rings. N—H and B—H FTIR vibrations in polyborazylene are reported at much higher wavenumbers[71] than those observed in the current work with strong and sharp peaks at 1450 and 780 cm^{-1} corresponding to a B_3N_3 ring structure.[59] These are absent from the FTIR of Ni/nano-AB ab/desorbed (Figure 7).

To clarify the possible structure of the oligomeric entity reversibly cycling hydrogen, first-principles density functional theory (DFT) calculations were performed. As summarized in Figure S12 in the Supporting Information, only hydrogen uptake and release involving simultaneously removal of hydrogen atoms along the backbone and at the end of the iminoborane oligomers chain, was found to display an energy of $\Delta E = +0.57$ eV, which lies within the range of desirable hydrogen binding energies leading to reversible H_2 storage, i.e., $0.1 < |\Delta E| < 1.0$ eV.[72,73] Calculations on polyborazylene type structures and polymeric structures involving a combination of cycling and linear (BH_xNH_x) units were found to be unstable upon the release of a single hydrogen atom. Taking into account these results in the context of the experimental evidences, it is thus apparent that the combination of Ni and AB at the nanosized led to the preferential formation of iminoborane oligomers involving $H—BN_2$ and $H—NB_2$ end chain sites leading to hydrogen reversibility (Scheme 2). In such a configuration, the highly dispersed Ni nanoparticles may also play an important role in facilitating the release and uptake of hydrogen from the end chains. Ni is well known for its ability to catalyze hydrogenation reactions including that of imine,[74,75] and the dehydrogenation of hydrocarbons in particular.[76] The occurrence of additional BN_3 sites by NMR further indicates that Ni/nano-AB ab/desorbed also contains cyclic $(BH_xNH_x)_n$ structures in addition to the linear iminoborane oligomers. If the formation of such cyclic structures could be minimized thus higher storage capacities would be feasible. The current system is also limited by hydrogen ab/desorption only occurring at the ends of the oligomer. Nevertheless, we foresee that by optimizing the length of these $(BHNH)_y$ iminoborane oligomers and finding ways to remove more hydrogen atoms along the backbone chain, the final hydrogen-storage capacity could be enhanced significantly. An iminoborane hexamer has a storage capacity of 1.2 mass% H_2 by considering the removal of hydrogen at the end of the chain only. Achieving full and reversibly removal of the hydrogen would lead to a storage capacity of 7.4 mass% H_2.

3. Conclusion

A novel and simple approach to control the properties of AB has been demonstrated and the drastic effect of such a strategy on the hydrogen storage properties of AB has been investigated. Via the modification of common antiprecipitation synthetic methods, the particle size of AB was successfully restricted to around 50 nm. Hydrogen desorption from these nanoparticles did not significantly differ from that of Bulk-AB. However, further reduction of $NiCl_2$ at the surface of the AB nanoparticles led to drastic improvements. Reaction of nanosized AB with $NiCl_2$ allowed the formation of metallic nickel nanoparticles (≈5 nm) forming a matrix embedding nanosized AB. The reduction of $NiCl_2$ at the surface of AB also led to a the formation of $[NH_4]^+[BCl_4]^-$, which is believed to act as a precursor enabling a controlled oligomerization of AB in the form of $[H_3NBH_2—NH_3]^+[BCl_4]^-$ compounds potentially leading to linear aminoborane and iminoborane oligomers upon the thermal decomposition of Ni/Nano-AB. Due to the combination of (a) catalytic effect of Ni, (b) nanoconfinement within the Ni matrix, and (c) modification of decomposition path upon exposure of the nanosized AB particles to $[NH_4]^+[BCl_4]^-$ resulting from the AB/$NiCl_2$ reduction process, problems associated with the melting of AB and formation of volatile by-products were drastically improved. Upon $NiCl_2$ reduction at the surface of the nanosized AB particles, the resulting nanosized Ni/AB matrix led to an onset for hydrogen as low as 50 °C and a significant reduction in the amount of volatile by-products. Only hydrogen was detected up to 100 °C. At higher temperatures, by products in the form of ammonia, diborane and borazine still remained. But this was nothing compared to the significant amount of volatiles released by Bulk-AB right from the beginning of its decomposition at 100 °C. More remarkably, the nanocomposite Ni/Nano-AB materials formed upon the reduction of $NiCl_2$ at the surface of the nanosized AB particles, led to the reversible release and uptake of hydrogen at 200 °C only and under a modest hydrogen pressure of 6 MPa. Only pure hydrogen was released from Ni/Nano-AB upon hydrogen cycling, but this was achieved with a relatively low reversible capacity of 1 mass% H_2 in comparison to the potential 13 mass% H_2 of Bulk-AB (when considering the two first decomposition steps, i.e., up to 250 °C). Further characterization by NMR, XPS, and FTIR assisted by first-principles DFT calculations indicate that an iminoborane oligomer resulting from the initial thermal decomposition of Ni/Nano-AB, is most likely the compound reversibly storing hydrogen, with the uptake and release occurring simultaneously at N and B sites in the backbone and ends of the chain of the oligomer. Such a restriction on the number of reversible hydrogen sites explains the low hydrogen storage capacity observed. However, the finding of reversibility along the decomposition path of AB demonstrates that reversible and low temperature H—B—N systems do exist. Beyond the demonstration of reversibility along the decomposition path of AB, the current findings open significant new avenues in the search of high capacity hydrogen storage materials based on light and relatively abundant elements for hydrogen storage on-board vehicles.

4. Experimental Section

Materials: Ammonia borane complex (NH_3BH_3, 97%) and oleic acid (99%) were purchased from Sigma-Aldrich. Nickel chloride ($NiCl_2$) was purchased from Ajax Finechem and dried under vacuum at 130 °C for

24 h before use. Cyclohexane and tetrahydrofuran (THF) was purchased as HPLC grade from Fisher Scientific and dried using a LC Technology SP-1 solvent purification system. All other chemicals were used without further purification. All operations were carried out under inert atmosphere in an Argon-filled LC-Technology glove box (<1 ppm O_2 and H_2O).

Synthesis of Ammonia Borane Nanoparticles: Nanosized particles of AB were synthesized by antiprecipitation methods following the method previously reported for the synthesis of sodium borohydride nanoparticles.[46] In a typical synthesis, 515 mg of ammonia borane complex was added in a small glass bottle with 2.5 mL of THF and heated to 45 °C. 5 mL of cyclohexane and 0.025 mL of oleic acid were added to a double jacketed flask and cooled to 15 °C. The ammonia borane solution was added to the cyclohexane solution dropwise with a dropping fuel. The mixture was aged at 15 °C under 500 rpm for 2 h. The resulting solution containing a white precipitate was collected and centrifuged to obtain a white solid. The solid was washed with cyclohexane twice and dried under vacuum at room temperature for 24 h. The material was denoted "Nano-AB".

Modification of Nano-AB with Ni: 100 mg of the as-synthesized AB nanoparticles was grinded in a mortar and placed in a small glass bottle. 45 mg of fine $NiCl_2$ powder was added to the bottle. The mixture is stirred under 250 rpm with a stirring bar at room temperature for 3 d. The resulting dark gray solid was characterized without further purification. The material was denoted "Nano-AB/Ni". Given the Ni content the theoretical hydrogen capacity was estimated to be of 13.2 mass%.

Modification of Bulk AB with Ni: As a reference commercially available AB (demoted Bulk-AB) was also modified with $NiCl_2$. 100 mg of commercial AB solids was mixed with 45 mg $NiCl_2$. The mixtures were grinded within an agate mortar to obtain a uniform light gray solid and further stirred at 250 rpm with a stirring bar at room temperature for 3 d.

Characterization: TEM, high resolution transmission electron microscopy, EDS, and selected area diffraction analysis was performed with a Philips CM200 field emission gun. TEM operated at 200 kV. The materials were dispersed in cyclohexane, sonicated, and dropped onto a carbon coated copper grid and dried in an argon filled glovebox before transfer to the microscope in a quick manner as to minimize air exposure. SEM analysis was performed using a FEI Nova NanoSEM 450 FE-SEM. Scanning transmission electron microscopy (STEM) was done in a probe-corrected JEOL ARM200F equipped with a cold field emission gun which provided an energy resolution <0.6 eV. The imagining was carried out at liquid nitrogen temperature, i.e., −196 °C, using a JEOL cooling holder. Annular dark-field (ADF) images were acquired with an inner and outer collection angle of 68 and 280 mrad, respectively. BF images were acquired with a collection angle of 11 mrad. STEM images were acquired with a dwell time of 10 µs. The microscope also featured a 100 mm^2 Centurio EDS detector, which combined with a high resolution pole-piece, featured almost ≈1 sr collection angle. Electron energy loss spectroscopy (EELS) was done using a GIF Quantum spectrometer. The collection angle for all EELS data was 6 mrad.

XRD was performed by using a PANalytical X'pert Multipurpose XRD system operated at 40 mA and 45 kV with a monochromated Cu Kα radiation (λ = 1.541 Å), step size = 0.01, 0.02, or 0.05, time per step = 10 or 20 s per step. The materials were protected against oxidation from air by a Kapton foil.

Hydrogen desorption profiles were acquired by TGA/DSC coupled with MS using a Mettler Toledo TGA/DSC 1 coupled with an Omnistar MS. Measurements were conducted at 10 °C min^{-1} under an argon flow of 20 mL min^{-1}. Masses between m/z = 2 and 100 were recorded.

Infrared analysis was carried out on a Bruker Vertex 70 V equipped with a Harrick diffuse reflectance infrared Fourier transform spectroscopy Praying Mantis accessory. The materials were loaded in an air-tight chamber in the glovebox and the chamber was fitted on the Praying Mantis. Spectra were acquired with a 1 cm^{-1} resolution with a MCT-detector.

The chemical properties of the surface of the nanoparticles were characterized by XPS using a Thermo Scientific ESCALAB250Xi, UK spectrometer (base pressure below 2.10^{-6} Pa). The sample pellets were prepared inside an Ar-filled glove box and quickly transferred to the spectrometer to minimize exposure to air. The XPS spectra were collected using a mono-chromatic Al Kα (1486.7 keV) X-ray source at 150 W power. Survey scans were collected at 100 eV pass energy with an energy step of 0.5 eV, while detailed scans were acquired at 20 eV pass energy and 0.1 eV energy step. The data were analyzed using the Advantage software.

The solid-state ^{11}B magic angle spinning NMR experiments were carried out on a narrow-bore Bruker Biospin Avance III solids-700 MHz spectrometer with a 16.4 Tesla superconducting magnet operating at a frequency of 224.7 MHz ^{11}B nucleus. Material of ≈3–10 mg was packed into 4 or 2.5 mm zirconia rotors fitted with Kel-f caps or Vespel caps, respectively. The 4 mm rotors were spun in a double resonance H—X probe head at 14 kHz at the magic angle, while the 2.5 mm rotors were spun to 30 kHz at the magic angle. The ^{11}B spectra were acquired with a hard 1 µs radio frequency pulse corresponding to a 30° tip angle. The recycle delay of 0.1 s was sufficient to ensure full relaxation of the ^{11}B signal and up to 100 K transients were co-added to ensure sufficient signal to noise. The spectra were obtained at room temperature and the ^{11}B chemical shifts were referenced to solid $NaBH_4$ at −42.5 ppm. The spectral deconvolution was carried out using the Dmfit software.[77]

Hydrogen cycling was characterized using a high pressure magnetic balance of 1 µg resolution equipped with capability for simultaneous density measurements (Rubotherm). The materials were first cycled at 100 and 200 °C and desorbed at 350 °C. Hydrogen cycling was then performed at 350 °C. 30 mg of material was used and a hydrogen pressure of 6 MPa for absorption and 0.01 MPa for desorption. With the high pressure balance, hydrogen uptake and release were determined from the weight changes. For an accurate determination of the amount of hydrogen stored, a blank measurement with the empty sample holder was performed at the cycling temperature to determine the mass and volume of the sample holder. Further measurements were performed at the cycling temperature under a He atmosphere with the material fully desorbed to determine the density of the materials and corresponding parameters for buoyancy corrections.

Computational Methods: First-principles calculations based on DFT were carried out in order to analyze the gas-storage and structural properties of B—N—H systems. Calculations were performed with the VASP code;[78,79] following the generalized gradient approximation to the exchange-correlation energy due to Perdew et al.,[80] and by taking into consideration long-range dispersion interactions through the Grimme scheme.[73,81] The "projector augmented wave" scheme was used to represent the ionic cores;[82] the electronic states 2s–2p of B atoms, the 2s–2p of N atoms, and the 1s of H atoms were treated as valence. Wave functions were represented in a plane-wave basis set truncated at 700 eV. Periodic boundary conditions were applied along all the dimensions of the simulation cell, and a vacuum slab of 20 Å thickness was introduced parallel to the Cartesian z–y plane in order to avoid spurious interactions with the neighboring images. The backbone of all considered polymers was always oriented along the Cartesian x direction. In the geometry relaxations, a force tolerance of 0.01 eV·$Å^{-1}$ was imposed in every atom. By using these parameters and dense k-point grids for integration within the Brillouin zone, total energies were obtained and converged to within 1 meV. Zero-point motion corrections to the energy were included in the results through the quasi-harmonic approximation.[83,84] The calculation of the vibrational phonon frequencies was performed with the direct method, as implemented in the PHON code.[83–85]

Supporting Information

Supporting Information is available from the Wiley Online Library or from the author.

Acknowledgements

Financial support by UNSW Internal Research Grant program is gratefully acknowledged along with the Office of Naval Research (Award No: ONRG-NICOP-N62909-16-1-2155). The authors appreciate the use of instruments in the Mark Wainwright Analytical Centre at UNSW as well as equipment funded by the Australian Research Council (ARC)-Linkage, Infrastructure, Equipment and Facilities (LIEF) grant LE120100104 located at the University of Wollongong. C.C. acknowledges financial support from the Australian Research Council's Future Fellowship funding scheme (No. FT140100135). Computational resources and technical assistance were provided by the Australian Government and the Government of Western Australia through Magnus under the National Computational Merit Allocation Scheme and The Pawsey Supercomputing Centre.

Conflict of Interest

The authors declare no conflict of interest.

Keywords

ammonia borane, hydrogen storage, nanosizing

Received: August 29, 2017
Revised: October 20, 2017
Published online:

[1] A. Gutowska, L. Li, Y. Shin, C. M. Wang, X. S. Li, J. C. Linehan, R. S. Smith, B. D. Kay, B. Schmid, W. Shaw, *Angew. Chem., Int. Ed.* **2005**, *44*, 3578.
[2] T. B. Marder, *Angew. Chem., Int. Ed.* **2007**, *46*, 8116.
[3] A. Staubitz, A. P. M. Robertson, I. Manners, *Chem. Rev.* **2010**, *110*, 4079.
[4] F. H. Stephens, V. Pons, R. T. Baker, *Dalton Trans.* **2007**, 2613.
[5] O. T. Summerscales, J. C. Gordon, *Dalton Trans.* **2013**, *42*, 10075.
[6] A. Rossin, M. Peruzzini, *Chem. Rev.* **2016**, *116*, 8848.
[7] M. Rakap, S. Özkar, *Int. J. Hydrogen Energy* **2010**, *35*, 1305.
[8] X. Kang, Z. Fang, L. Kong, H. Cheng, X. Yao, G. Lu, P. Wang, *Adv. Mater.* **2008**, *20*, 2756.
[9] T. He, Z. Xiong, G. Wu, H. Chu, C. Wu, T. Zhang, P. Chen, *Chem. Mater.* **2009**, *21*, 2315.
[10] X.-l. Si, L.-x. Sun, F. Xu, C.-l. Jiao, F. Li, S.-s. Liu, J. Zhang, L.-f. Song, C.-h. Jiang, S. Wang, *Int. J. Hydrogen Energy* **2011**, *36*, 6698.
[11] S. Sepehri, B. B. Garcia, G. Cao, *J. Mater. Chem.* **2008**, *18*, 4034.
[12] J.-M. Yan, X.-B. Zhang, S. Han, H. Shioyama, Q. Xu, *J. Power Sources* **2009**, *194*, 478.
[13] T. J. Clark, G. R. Whittell, I. Manners, *Inorg. Chem.* **2007**, *46*, 7522.
[14] A. Paul, C. B. Musgrave, *Angew. Chem.* **2007**, *119*, 8301.
[15] M. C. Denney, V. Pons, T. J. Hebden, D. M. Heinekey, K. I. Goldberg, *J. Am. Chem. Soc.* **2006**, *128*, 12048.
[16] S. Basu, A. Brockman, P. Gagare, Y. Zheng, P. V. Ramachandran, W. N. Delgass, J. P. Gore, *J. Power Sources* **2009**, 238.
[17] N. Blaquiere, S. Diallo-Garcia, S. I. Gorelsky, D. A. Black, K. Fagnou, *J. Am. Chem. Soc.* **2008**, *130*, 14034.
[18] Y. Yang, F. Zhang, H. Wang, Q. Yao, X. Chen, Z.-H. Lu, *J. Nanomater.* **2014**, *2014*, 3.
[19] Ö. Metin, V. Mazumder, S. Özkar, S. Sun, *J. Am. Chem. Soc.* **2010**, *132*, 1468.
[20] L. Yang, W. Luo, G.-Z. Cheng, *Catal. Lett.* **2013**, *143*, 873.
[21] G. Moussa, R. Moury, U. B. Demirci, T. Şener, P. Miele, *Int. J. Energ. Res.* **2013**, *37*, 825.
[22] M. G. Hu, R. A. Geanangel, W. W. Wendlandt, *Thermochim. Acta* **1978**, *23*, 249.
[23] V. Sit, R. Geanangel, W. Wendlandt, *Thermochim. Acta* **1987**, *113*, 379.
[24] G. Wolf, J. Baumann, F. Baitalow, F. Hoffmann, *Thermochim. Acta* **2000**, *343*, 19.
[25] K. Shimoda, K. Doi, T. Nakagawa, Y. Zhang, H. Miyaoka, T. Ichikawa, M. Tansho, T. Shimizu, A. K. Burrell, Y. Kojima, *J. Phys. Chem. C* **2012**, *116*, 5957.
[26] F. Baitalow, J. Baumann, G. Wolf, K. Jaenicke-Rößler, G. Leitner, *Thermochim. Acta* **2002**, *391*, 159.
[27] J. Baumann, F. Baitalow, G. Wolf, *Thermochim. Acta* **2005**, *430*, 9.
[28] M. E. Bluhm, M. G. Bradley, R. Butterick, U. Kusari, L. G. Sneddon, *J. Am. Chem. Soc.* **2006**, *128*, 7748.
[29] F. Cheng, H. Ma, Y. Li, J. Chen, *Inorg. Chem.* **2007**, *46*, 788.
[30] A. Feaver, S. Sepehri, P. Shamberger, A. Stowe, T. Autrey, G. Cao, *J. Phys. Chem. B* **2007**, *111*, 7469.
[31] L. Li, X. Yao, C. Sun, A. Du, L. Cheng, Z. Zhu, C. Yu, J. Zou, S. C. Smith, P. Wang, *Adv. Funct. Mater.* **2009**, *19*, 265.
[32] Z. Li, G. Zhu, G. Lu, S. Qiu, X. Yao, *J. Am. Chem. Soc.* **2010**, *132*, 1490.
[33] H. Yang, Z. Li, K. Liu, F. Meng, C. Niu, *J. Phys. Chem. C* **2015**, *119*, 2260.
[34] L. Zhang, G. Xia, Y. Ge, C. Wang, Z. Guo, X. Li, X. Yu, *J. Mater. Chem. A* **2015**, *3*, 20494.
[35] T. Hügle, M. Hartl, D. Lentz, *Chem. Eur. J.* **2011**, *17*, 10184.
[36] D. Kumar, H. A. Mangalvedekar, S. K. Mahajan, *Mater. Renew. Sust. Energy* **2014**, *3*, 1.
[37] S. B. Kalidindi, B. R. Jagirdar, *J. Indian Inst. Sci.* **2010**, *90*, 181.
[38] A. C. Gangal, P. Kale, R. Edla, J. Manna, P. Sharma, *Int. J. Hydrogen Energy* **2012**, *37*, 6741.
[39] D. A. Dixon, M. Gutowski, *J. Phys. Chem. A* **2005**, *109*, 5129.
[40] M. Gutowski, T. Autrey, *Prepr. Pap.-Am. Chem. Soc., Div. Fuel Chem.* **2004**, *49*, 275.
[41] S. Frueh, R. Kellett, C. Mallery, T. Molter, W. S. Willis, C. King'ondu, S. L. Suib, *Inorg. Chem.* **2011**, *50*, 783.
[42] U. B. Demirci, S. Bernard, R. Chiriac, F. Toche, P. Miele, *J. Power Sources* **2011**, *196*, 279.
[43] N. M. Yoon, C. S. Pak, C. Brown Herbert, S. Krishnamurthy, T. P. Stocky, *J. Org. Chem.* **1973**, *38*, 2786.
[44] H.-J. Himmel, H. Schnöckel, *Chem. Eur. J.* **2002**, *8*, 2397.
[45] C. R. Miranda, G. Ceder, *J. Phys. Chem.* **2007**, *126*, 184703.
[46] M. L. Christian, K. F. Aguey-Zinsou, *ACS Nano* **2012**, *6*, 7739.
[47] M. Christian, K.-F. Aguey-Zinsou, *Chem. Commun.* **2013**, *49*, 6794.
[48] R. Benzouaa, U. B. Demirci, R. Chiriac, F. Toche, P. Miele, *Thermochim. Acta* **2010**, *509*, 81.
[49] S. B. Kalidindi, J. Joseph, B. R. Jagirdar, *Energy Environ. Sci.* **2009**, *2*, 1274.
[50] S. B. Kalidindi, U. Sanyal, B. R. Jagirdar, *Inorg. Chem.* **2010**, *49*, 3965.
[51] S. W. Stafford, R. B. McLellan, *Scr. Metall. Mater.* **1975**, *9*, 1195.
[52] J. Liu, S. Z. Qiao, J. S. Chen, X. W. Lou, X. Xing, G. Q. Lu, *Chem. Commun.* **2011**, *47*, 12578.
[53] R. G. Chaudhuri, S. Paria, *Chem. Rev.* **2012**, *112*, 2373.
[54] Y. Wang, J. He, C. Liu, W. H. Chong, H. Chen, *Angew. Chem., Int. Ed.* **2015**, *54*, 2022.
[55] K. D. Gilroy, A. Ruditskiy, H.-C. Peng, D. Qin, Y. Xia, *Chem. Rev.* **2016**, *116*, 10414.
[56] Y. Li, F. Fang, Y. Song, Y. Li, Q. Zhang, L. Ouyang, M. Zhu, D. Sun, *Int. J. Hydrogen Energy* **2012**, *37*, 4274.
[57] A. C. Stowe, W. J. Shaw, J. C. Linehan, B. Schmid, T. Autrey, *Phys. Chem. Chem. Phys.* **2007**, *9*, 1831.

[58] W. J. Shaw, M. Bowden, A. Karkamkar, C. J. Howard, D. J. Heldebrant, N. J. Hess, J. C. Linehan, T. Autrey, *Energy Environ. Sci.* **2010**, *3*, 796.
[59] D.-P. Kim, K.-T. Moon, J.-G. Kho, J. Economy, C. Gervais, F. Babonneau, *Polym. Adv. Technol.* **1999**, *10*, 702.
[60] R. A. Geanangel, J. W. Rabalais, *Inorg. Chim. Acta* **1985**, *97*, 59.
[61] S. I. Tanase, D. Tanase, M. Dobromir, A. V. Sandu, V. Georgescu, *J. Supercond. Novel Magn.* **2016**, *29*, 469.
[62] H. Schmiers, J. Friebel, P. Streubel, R. Hesse, R. Köpsel, *Carbon* **1999**, *37*, 1965.
[63] C. Petit, M. Seredych, T. J. Bandosz, *J. Mater. Chem.* **2009**, *19*, 9176.
[64] A. Stock, E. Pohland, *Ber. Dtsch. Chem. Ges.* **1926**, *59*, 2210.
[65] C. Gervais, J. Maquet, F. Babonneau, C. Duriez, E. Framery, M. Vaultier, P. Florian, D. Massiot, *Chem. Mater.* **2001**, *13*, 1700.
[66] E. A. Il'inchik, V. V. Volkov, L. N. Mazalov, *J. Struct. Chem.* **2005**, *46*, 523.
[67] W. Lei, V. N. Mochalin, D. Liu, S. Qin, Y. Gogotsi, Y. Chen, *Nat. Commun.* **2015**, *6*, 8849.
[68] P. J. Fazen, E. E. Remsen, J. S. Beck, P. J. Carroll, A. R. McGhie, L. G. Sneddon, *Chem. Mater.* **1995**, *7*, 1942.
[69] T. Kobayashi, S. Gupta, M. A. Caporini, V. K. Pecharsky, M. Pruski, *J. Phys. Chem. C* **2014**, *118*, 19548.
[70] D. Jacquemin, *J. Phys. Chem. A* **2004**, *108*, 9260.
[71] C. Zou, C. Zhang, B. Li, S. Wang, Z. Xie, Y. Song, *Mater. Sci. Eng. A* **2015**, *620*, 420.
[72] J. Li, T. Furuta, H. Goto, T. Ohashi, Y. Fujiwara, S. Yip, *J. Chem. Phys.* **2003**, *119*, 2376.
[73] C. Cazorla, *Coord. Chem. Rev.* **2015**, *300*, 142.
[74] B. Chen, U. Dingerdissen, J. G. E. Krauter, H. G. J. Lansink Rotgerink, K. Möbus, D. J. Ostgard, P. Panster, T. H. Riermeier, S. Seebald, T. Tacke, H. Trauthwein, *Appl. Catal.* **2005**, *280*, 17.
[75] J. Volf, J. Pašek, *Stud. Surf. Sci. Catal.* **1986**, *27*, 105.
[76] J. H. Sinfelt, J. L. Carter, D. J. C. Yates, *J. Catal.* **1972**, *24*, 283.
[77] D. Massiot, F. Fayon, M. Capron, I. King, S. Le Calvé, B. Alonso, J.-O. Durand, B. Bujoli, Z. Gan, G. Hoatson, *Magn. Reson. Chem.* **2002**, *40*, 70.
[78] G. Kresse, J. Furthmüller, *Phys. Rev. B* **1996**, *54*, 11169.
[79] G. Kresse, D. Joubert, *Phys. Rev. B* **1999**, *59*, 1758.
[80] J. P. Perdew, K. Burke, M. Ernzerhof, *Phys. Rev. Lett.* **1996**, *77*, 3865.
[81] S. Grimme, *J. Comput. Chem.* **2004**, *25*, 1463.
[82] P. E. Blöchl, *Phys. Rev. B* **1994**, *50*, 17953.
[83] C. Cazorla, J. Boronat, *Phys. Rev. B* **2015**, *91*, 024103.
[84] C. Cazorla, J. Iniguez, *Phys. Rev. B* **2013**, *88*, 214430.
[85] D. Alfe, *Comput. Phys. Commun.* **2009**, *180*, 2622.
[86] C. W. Hamilton, R. T. Baker, A. Staubitz, I. Manners, *Chem. Soc. Rev.* **2009**, *38*, 279.
[87] V. Pérez-Dieste, O. Castellini, J. Crain, M. Eriksson, A. Kirakosian, J.-L. Lin, J. McChesney, F. Himpsel, C. Black, C. Murray, *Appl. Phys. Lett.* **2003**, *83*, 5053.
[88] D. H. Lee, R. A. Condrate, W. C. Lacourse, *J. Mater. Sci.* **2000**, *35*, 4961.

